Wave field measurements of regular wave–monopile interaction using Free-Surface Synthetic Schlieren

Oldenziel, G.; Moreno-Rodenas, A.; Bruinsma, N.; Bakker, W.

RESEARCH ARTICLE

Wave field measurements of regular wave–monopile interaction using Free-Surface Synthetic Schlieren

G. Oldenziel[1,2] · A. Moreno-Rodenas[1] · N. Bruinsma[1] · W. Bakker[1]

Abstract

Spatio-temporal wave patterns due to wave field–structure interaction can be very complex to measure and analyze when using (intrusive) point probes. Free-surface field measurements can offer much needed insight in this domain. Nevertheless, to the best of the authors' knowledge, these methods are rarely used in experimental offshore engineering and research. In these fields, typical domain sizes are at least in the order of several m^2, whereas (optical) free-surface field measurements are often not performed in domains with dimensions larger than roughly 0.5×0.5 m^2. In the current work, the optical free-surface measurement technique named Free-Surface Synthetic Schlieren (FS-SS) is applied to measure the interaction between an incident wave field and a surface piercing cylinder, or monopile, in a domain of several m^2 for the first time. The FS-SS method is validated for wave fields with wavelengths $\lambda \ll L$ to $\lambda \gg L$, where L is the domain size in the direction of wave propagation. It is found that the incorporation of an additional water level measurement improves the agreement between intrusive wave height meters and the FS-SS measurement for large wavelengths ($\lambda/L > 0.5$) as compared to assuming a zero-mean free-surface. Wave field–monopile interaction is measured for two values of D/λ: $D/\lambda = 0.1$ and $D/\lambda = 0.2$, where D is the monopile diameter. For the case $D/\lambda = 0.2$ the interaction wave field is analyzed by subtracting the measured wave field in the absence of a structure, from the measured interaction wave fields. The measured difference wave field reveals many interaction phenomena such as locations of amplification, both near the monopile and further away, a wake that has certain similarities with a Kelvin wake, and a circular small wavelength diffraction pattern. Additionally, the embedding of the measurements in a wave breaking regime map is presented. In this map, the applicability for certain wave conditions can be clearly visualized. It is concluded that the FS-SS method, including the proposed improvement using additional sensor data, is a useful addition to the toolbox of hydraulic engineers and researchers, and that especially the measured locations of wave amplification in the far field will not be easily detected using (arrays of) point probes.

1 Introduction

Despite the significant progress in recent years in (optical) techniques to measure water wave fields (Settles et al. 2017; Moisy et al. 2009; Gomit et al. 2022), it is remarkable how rarely these techniques are applied in experimental work for offshore engineering applications. Specifically for the quantification of complex wave fields, free-surface field measurements can help in the identification of spatio-temporal patterns of relevance which point probes alone often do not resolve. Examples are the wave fields that occur due to wave–structure interaction, for example wave generation due to calving ice bergs (Heller et al. 2019) or the interaction of a wave with a surface piercing cylinder, or monopile. Here, monopile is short for 'monopile foundation for offshore structure.' The interaction between an incident wave field and a monopile is currently one of the most practically

✉ G. Oldenziel
Gosse.Oldenziel@Deltares.nl; g.oldenziel@tudelft.nl

A. Moreno-Rodenas
antonio.morenorodenas@deltares.nl

N. Bruinsma
niek.bruinsma@deltares.nl

W. Bakker
wout.bakker@deltares.nl

1   Hydraulic Engineering Unit, Deltares, Delft,
     The Netherlands

2   Laboratory for Aero- and Hydrodynamics, Faculty of 3Me,
     Delft University of Technology, Delft, The Netherlands

relevant and fundamental wave fields. The diffraction of waves on a monopile has often been modeled (Stansberg and Kristiansen 2005, Chau and Eatock Taylor 1992, Malenica and Molin 1995), in many cases however, poor agreement has been found between measurements and first- and second-order diffraction solutions (Stansberg and Kristiansen 2005). In the literature, two types of nonlinear interactions have been described that can may cause a significant increase in crest elevation in waves around monopile structures (see e.g., Sheikh and Swan 2005; Swan and Sheikh 2015). Phenomena arising from these interactions are suspected to have led to damage on several Gravity-Based Structures (GBS) in the North Sea (Sheikh and Swan 2005; Swan and Sheikh 2015). Although extreme waves themselves are not in the current scope, the ability to measure wave fields in a synoptical manner in the laboratory, including nonlinear interactions, is important for the further development of the understanding of all aspects of wave field–structure interaction, including quantification of the wave facility behavior itself.

For the measurement of wave fields in laboratory setups, there are several optical techniques available to the experimentalist. Optical wave field measurement methods can be subdivided in the categories of refraction based, stereo-correlation based, or projection based. For the refraction-based methods often the apparent displacement of an image pattern (for example mounted on the floor of a tank or basin) due to refraction is quantified and correlated to the free-surface gradient field which can possibly be integrated to obtain the free-surface field. Stereo correlation-based methods seek to determine the three-dimensional world position of particles or features. In projection-based methods, a pattern (sometimes a line) is projected on the liquid surface and from via detection of (features of) the pattern on the free-surface topographical features can be obtained. A recent overview of the different methods is given in (Van Meerkerk et al. 2020). An example of a stereoscopic imaging-based method for a very large domain (35×35 m^2) is presented in Benetazzo et al. (2012). For the stereo-matching to work using this technique, it is assumed that enough structure on the free surface should be present. It is not known if this is the case in transparent water in a laboratory facility. Several laser-based methods are presented in (Van Meerkerk et al. 2020, in the main presented method herein fluorescent dye is added to the fluid in addition to performing laser scanning). In Table 1, a selection of methods is shown and tabulated by principle, properties and demands on equipment. Gomit et al. (2015) report the reconstruction of a stationary wave field of 4×8 m^2, and in Gomit et al. (2013) a free surface of 0.2×6.7 m^2 is reconstructed by appending successive free-surface measurements of approximately 0.20×0.20 m^2. In the same work, data are presented where the instantaneous measured area is 0.4×0.5 m^2 with a stereoscopic reconstruction method described by Chatellier et al. (2013).

Table 1 Principle, properties and necessary instrumentation for different free-surface measurement methods

| Method	Principle	Measured quantities	Domain dimensions (m²)	Instrumentation
Benetazzo et al. (2012)	Stereoscopic correlation	Free-surface $\eta(x,y)$ 15 Hz	35×35	2 synchronized CCD cameras
Gomit et al. (2015)	Projection based/Stereoscopic reconstruction	Free-surface $\eta(x,y)$ stationary	4×8	2 synchronized cameras, custom laser projection system
Van Meerkerk et al. (2020)	Projection based/Stereoscopic reconstruction	Free-surface $\eta(x,y)$ 53 Hz	0.120×0.062	3 synchronized high-speed cameras, high speed laser, oscillating mirror
Kolaas et al. (2018)	Refraction based (differential apparent dot displacement)	Free-surface gradient $d\eta/dx(x,y)$ is measured. Free-surface $\eta(x,y)$ is determined via integration (frame rate not reported, only rate of illumination 30 Hz)	0.30×0.10	Visual/NIR camera (2 sensors), telecentric lens, blue LED, infrared LED, cold mirror
Savelsberg et al. (2006)	Refraction based (Position of surface refracted laser spot is measured.)	Free-surface gradient $d\eta/dx(x)$ is quantified along a line (100 Hz)	0.05 (line measurement)	He–Ne Laser, optics, oscillating mirror, frosted glass, Position Sensing Device
Moisy et al. (2009)	Refraction based (Apparent dot displacement is measured)	Free-surface gradient $d\eta/dx(x,y)$ is measured. Free-surface $\eta(x,y)$ is determined via integration (100 Hz)	0.2×0.2	Camera
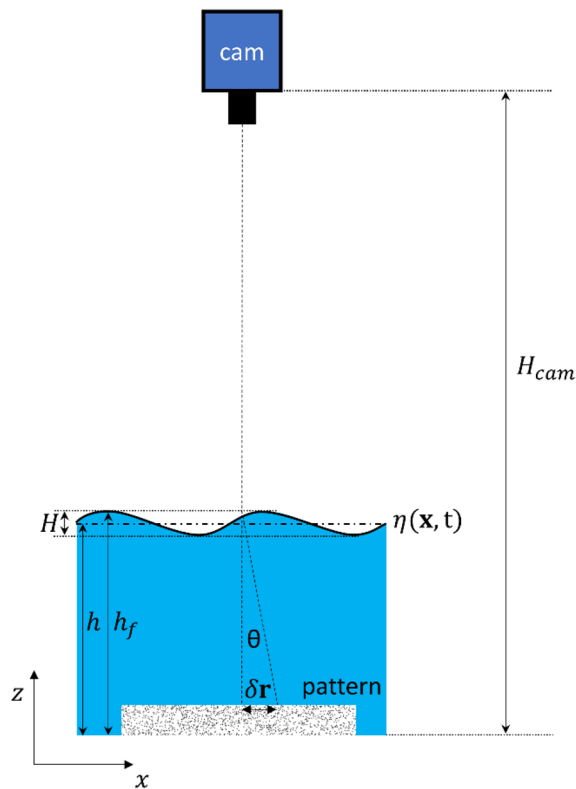
Fig. 1 Sketch of experimental setup for FS-SS. Indicated are wave-profile η (relative to still water level h), wave height H, still water level h, camera height H_{cam}, free-surface level h_f, apparent displacement δr and angle of refraction θ

Moisy et al. (2009) describe a refraction-based wave field reconstruction method referred to as Free-Surface Synthetic Schlieren (FS-SS). With this method, a camera is typically located above the free surface of the area of interest and a given pattern (i.e., a random dot pattern) is displayed at the bottom of a free surface. Images are recorded from above, and the apparent displacement of the pattern due to refraction is determined using image cross-correlation techniques (Adrian et al. 2011). Under some assumptions, the virtual displacement is found to be proportional to the free-surface gradient. A sketch of a typical experimental setup is shown in Fig. 1.

Upon integrating the gradient field, the free-surface interface geometry is obtained. Note that the free-surface gradient field can, in principle, also be measured in a different manner, see for example Savelsberg et al. 2006, where the free-surface gradient is measured along a line at a temporal frequency of O(100 Hz) using a Position Sensing Device to quantify the location of a refracted laser dot that is scanned along the measurement line. An advantage of this type of measurement is that a relatively high-speed measurement can be performed over a longer period of time than for high-speed cameras, where the memory limit is an

issue. In this way also low-frequency components can be measured. The FS-SS method has some attractive properties when compared to other optical-based measuring methods, firstly no laser safety measures are necessary, secondly the least-squares numerical integration methods that is applied, is known to be robust and stable (Proot et al. 2002, De Maerschalck et al. 2005). Li et al. 2021 present a synthetic Schlieren method where the equations linking the virtual displacement with the gradient field are solved using the Newton–Raphson method. A reference height is then no longer needed. Kolaas et al. 2018 describe a variant of the FS-SS method where they use multiple wavelengths of light to attain a higher accuracy of the free-surface field measurement particularly for high free-surface gradients, in a domain of 0.30×0.10 m^2. The improvement of the measured steep gradients comes at the cost of the use of a specialized visual/NIR camera and the need for sufficient illumination in both parts of the spectrum, which is not always practically feasible, especially in domains lacking an optically transparent floor. In their work, Kolaas et al. 2018 also present a measurement of the impact of a focused wave on a monopile. Because of the attractive properties for implementation for domain dimensions of interest to off-shore engineering in a hydraulic laboratory, in the current work the free-surface field for wave–monopile interaction will be measured using FS-SS. Thus, the objective of the current paper is to provide hydraulic and offshore engineers with a quantitative comparison of the measurement results with depth gauge data, and concrete guidelines for the application of wave field measurements using FS-SS for domain dimensions in the order of meters, aimed at wave fields around offshore structures.

The paper is organized as follows: in Sect. 2 a short overview of the experimental setup and the present implementation of the FS-SS method are given. In Sect. 3, the FS-SS method is validated by comparing to intrusive wave gauge measurements. In Sect. 4 results for the wave–monopile interaction are presented and discussed. In Sect. 5, the conclusions are drawn and recommendations are given.

2 Experimental setup and method

2.1 Experimental setup

The measurements are performed in the Atlantic basin facility, located at Deltares (Delft, The Netherlands). This wave flume is designed to allow for simultaneous wave and current generation, see for example Paulsen et al. (2019). Images of the experimental setup are shown in Fig. 2 and a sketch is shown in Fig. 3. The facility consists of a 75 m long, 8.7 m wide and 1.0 m deep flume. Waves are generated with a piston-type wave maker, which is equipped with
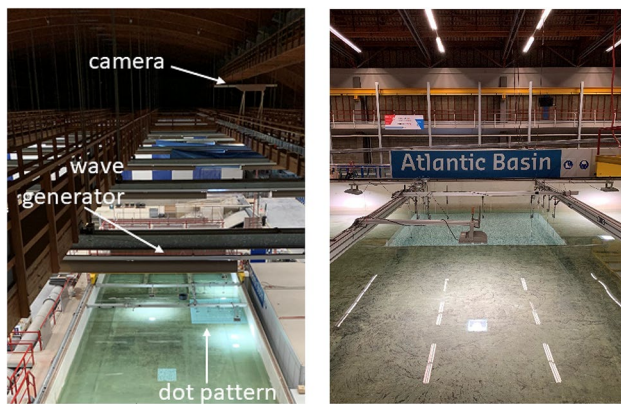
Fig. 2 Images of the experimental setup (without monopile present). Left: top view looking toward the wave maker. Right: image of the random dot pattern, looking from the side of the basin. The structural beams carrying the wave gauges and the lights are visible in the image

rods are oriented such that the distance to the upstream wave maker board is identical. Two wave height meters consist of three rods. The wave height sensors measurement principle is based on resistivity. An alternating current is imposed on one rod and the resulting voltage on the other rod (and thus the resistance of the water layer in between the rods) is measured. The lower the water level is, the higher the resistance. To compensate for possible changes in resistivity of the water also a reference signal over a platinum electrode, located at the lowermost position of the rods, is measured. This electrode is always located under water. The wave height sensors are calibrated before the measurements and are nulled every day before the start of the measurements. The signal is low pass filtered with a cutoff frequency of 20 Hz before being digitized. The wave height sensors have a static accuracy that is 0.5% of the measurement range of the sensor (0.50 m). The sensor data that are used to compare to the FS-SS reconstruction is measured using four wave
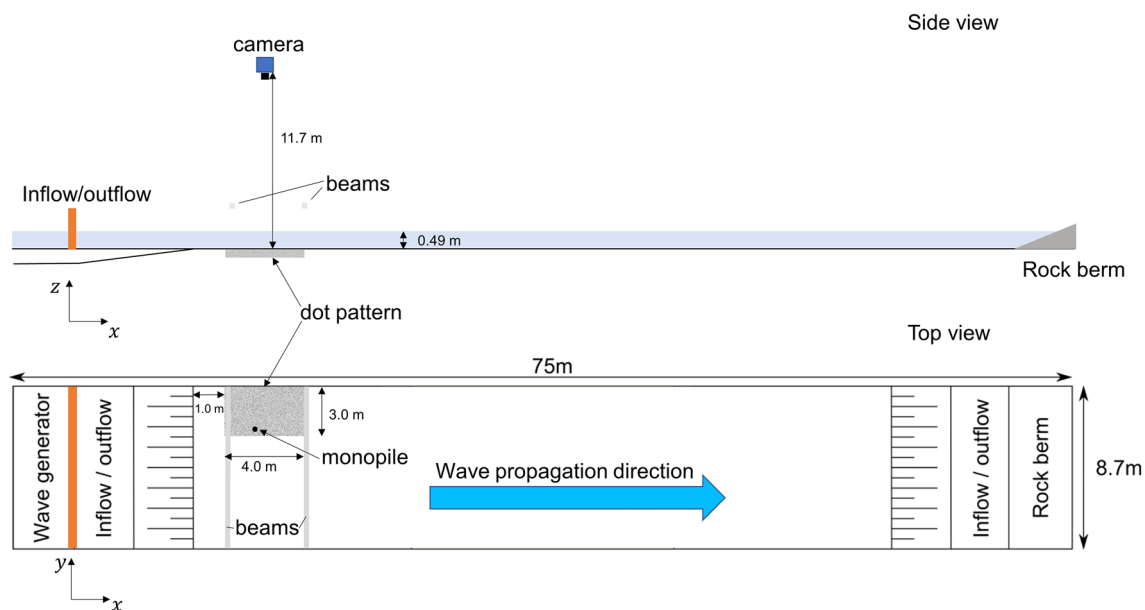

Fig. 3 Top: sketch of experimental setup (side view). Bottom: sketch of experimental setup (top view)

both Active Reflection Compensation (ARC) and second order wave generation. A rectangular patch of 4.0×3.0 m² (streamwise × transverse) at approximately 8.55 m downstream of the wave maker, is equipped with a random dot pattern on the floor of the basin. Fifteen wave height sensors, thirteen of which consisting of two 0.590 m high, 4 mm diameter stainless steel rods[1] with a spacing of 24.3 mm, are mounted at the non-wall sides of the random dot pattern. The

gauges, at a streamwise location of x/L = 0.01, x/L = 0.14, x/L = 0.27, and x/L = 0.51 of the FS-SS domain streamwise dimension of L = 3.37 m. The locations of the wave gauges are indicated in Fig. 4, and an image of the setup including monopile is shown. The acrylic monopile has an external diameter of D = 200 mm and is located at (x/L, y/L) = (0.378, 0.0743). The wave gauge signal is sampled at 1000 Hz, this sampling rate is relatively high but is chosen such that a drift between the clocks of the image acquisition system is taken into account. The camera trigger signal is a TTL pulse of 5 µs and is elongated using a signal processing

Fig. 4 Left: raw image with location of wave gauges. Right: raw image for wave–monopile interaction measurements, the inset shows a 32×32 px region with dots. The incident wave direction in the images is from below
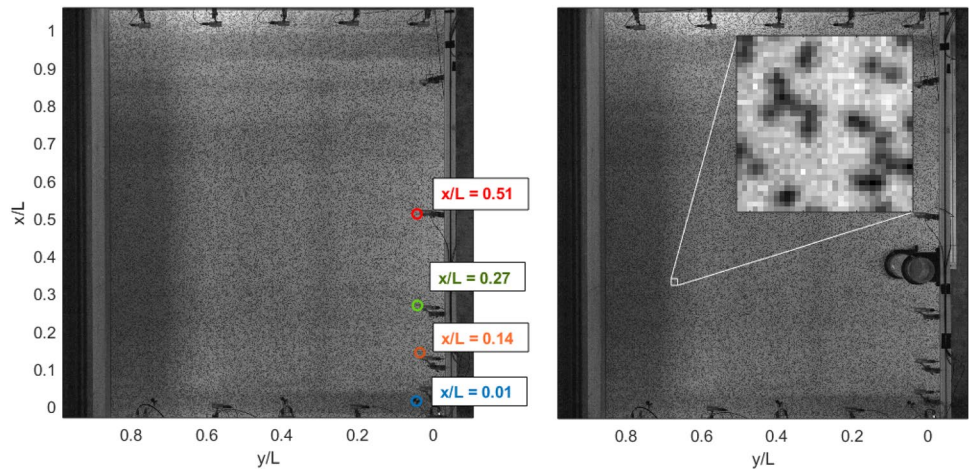
unit to be 10 ms (in order to be accurately measurable in the data acquisition).

At an elevation of $H_{cam} = 11.7$ m above the random dot pattern a digital camera (LaVision ImagerMX 4 M, 2048×2048 pixel) with a CMOS sensor and a bit depth of 10 bit is imaging the field of view. The pixel size is 5.5×10^{-6} m. The applied frame rate is 25 Hz. An objective with a focal length of 35 mm (Fujinon HF35SA-1) is mounted on the camera. The aperture was set at f$^{\#}$ 5.6. The exposure time is 10×10^{-3} s. The calibration is performed using the third order polynomial method as described in (Soloff et al. 1997). A plate of 4.0×3.0 m^2 with circular dots is used for the calibration.

The thickness of the stainless-steel plate on which the pattern is attached using adhesive spray is 1.0×10^{-3} m. The dots have a diameter of 9.0×10^{-3} m and consist of three concentric circles with decreasing grey value toward the dot center and are generated using the PIVMAT toolbox as described in (Moisy et al. 2009). The pattern consists of approximately 120,000 dots and is printed on a polyester film that is attached onto the stainless-steel plates using adhesive spray. Due to the finite paraxial angle of the camera and objective, combined with the maximum attainable camera elevation, the imaged part of the dot pattern is 3.8×3.0 m. In order to prevent interference of the image of the wave gauges with the dot pattern, the part of the domain on which FS-SS processing is performed is 3.37×2.35 m^2 and is the part of the image in between the wall and a large part of the wave height sensors. Aluminum beams used to mount wave height sensors are placed transversely over the flume directly outside of the view of the camera up- and downstream of the field of view.

In order to perform the image cross-correlation, images of the refracted dot pattern should be without motion blur while having significant contrast, implying that there should be enough light. A limiting feature is that direct reflections of hall lights on the free surface render the dot pattern undetectable at the location of the reflection. To attain the best image quality possible, only the hall lights that lead to direct reflections are masked physically. To increase the luminosity, three local lights are added to the setup outside the field of view at approximately 0.30 m above the free surface, see Fig. 2.

2.2 Image cross-correlation processing

A reference image is recorded where the basin is fully at rest before the measurements. During the measurement process, images are acquired at a rate of 25 Hz. The apparent displacement field is determined via cross-correlation of the images with the reference image. A geometric mask and a min–max filter are applied to the raw images after which the multi pass image correlation is performed with the first pass at a window size of 64×64 pixels with 50% overlap and the final two passes at a window size of 16×16 pixels with 50% overlap. This leads to a vector spacing of 14.3 mm. For vector validation a peak ratio of 1.5 is required between the highest and second highest correlation peak and universal outlier detection is applied where a maximum residual of 2 is allowed. Invalid vectors are replaced by a linearly interpolated vector. The percentage of valid vectors is typically larger than 95%. The processing is performed using Davis software version 8 and version 10.

2.3 FS-SS method and processing

From the measured displacement fields the free-surface gradient field is calculated as:

$$\nabla h_f = \frac{-\delta \boldsymbol{r}}{h^*}$$

(Moisy et al. 2009), here h_f is the free-surface elevation, $\delta \boldsymbol{r}$ is the apparent displacement and h* is a constant, defined via $\frac{1}{h^*} = \frac{1}{\alpha h} - \frac{1}{H_{cam}}$, and here equal to h*$=0.119$.

Table 2 Wave conditions for FS-SS validation measurements. Here, Fr_c indicates the dimensionless wave celerity, H/h the relative wave height, $T\sqrt{g/h}$ the dimensionless wave period, λ_{calc}/L the wavelength relative to domain length, h/λ_{calc} the still water level over the wave-length, D/λ_{calc} indicates the monopile diameter over the wavelength, K_C is the Keulegan Carpenter number. The dimensional wave height and wave period are given by H and T, the duration of the measurement by 'Time' and the wave type is given in the final column

Fr_c (-)	H/h (-)	$T\sqrt{g/h}$ (-)	λ_{calc}/L (-)	h/λ_{calc} (-)	K_C (-)	D/λ_{calc} (-)	H (mm)	T (s)	Time (s)	Wave type
0.37	0.038 ± 0.005	2.4	0.13	1.1	–	–	18.6 ± 2.5	0.53	40	Deep
0.58	0.054 ± 0	3.6	0.31	0.49	0.42	0.20	26.4 ± 0.2	0.8	40	Intermediate
	0.176 ± 0.002	3.6	0.33	0.49	–	–	85.9 ± 1.0	0.8	40	Intermediate
0.79	0.008 ± 0.002	5.4	0.67	0.24	–	–	3.9 ± 0.9	1.2	25	Intermediate
	0.175 ± 0.001	5.4	0.65	0.24	1.5	0.10	85.4 ± 0.4	1.2	40	Intermediate
	0.219 ± 0.001	5.4	0.63	0.24	–	–	107 ± 0.4	1.2	40	Intermediate
	0.261 ± 0.001	5.4	0.63	0.24	–	–	127 ± 1	1.2	40	Intermediate
0.86	0.193 ± 0.001	6.7	0.86	0.17	–	–	94.2 ± 0.2	1.5	40	Intermediate
	0.288 ± 0.001	6.7	0.86	0.17	–	–	141 ± 0	1.5	40	Intermediate
0.97	0.210 ± 0.001	14.8	2.10	0.069	–	–	103 ± 0	3.3	40	Intermed./shallow
	0.339 ± 0.002	14.8	2.10	0.069	–	–	166 ± 1	3.3	40	Intermed./shallow

This free-surface gradient field is subsequently integrated using Least-Squares (LS) integration to determine relative heights. See Appendix 1 for a brief summary of the LS integration method. In the current work, the integration is performed in two ways for all regular wave measurements. In the first implementation it is assumed that the mean of the elevation field is equal to zero. In the second implementation, here referred to as 'data fusion', the absolute free-surface level is supplied from the wave gauge measurement at x/L = 0.51 via addition:

$$\Delta(x_{WG}, t) = \eta_{WG}(x_{WG}, t) - \eta_{FS-SS}(x_{WG}, t),$$
$$\eta(x, t) = \eta_{FS-SS}(x, t) + \Delta(x_{WG}, t).$$

These operations are performed using the PIVMAT MATLAB library supplied by (Moisy et al. 2009).

In the results section, time signals as measured using the wave gauges are compared to the time varying wave height as reconstructed using FS-SS at the location of wave gauges as indicated in Fig. 4. The signals are compared at the first sample of each acquired camera pulse. The determination of the correct grid point from which to extract the water level is performed every time-step by taking the point nearest to the wave gauge location.

In the regular wave–monopile interaction, the LS integration can lead to inaccuracies in the wave fields near the monopile. It is found that replacing the (zero) virtual displacement in the monopile region by extrapolating the regular wave displacement into the monopile region largely eliminates differences between the gradient of the reconstructed wave field and $-\delta\mathbf{r}/h^*$.

3 Validation of FS-SS method

3.1 Experimental conditions

In the current work, the wave height is defined as:

$$H = \eta_{max} - \eta_{min}$$

where η is the free-surface elevation relative to the mean water level, and η_{min} and η_{max} denote the minimum and maximum wave height for each individual wave period. The still water level is denoted as h. Regular wave fields are generated at five different values of the Froude number $Fr_c = c/\sqrt{gh}$, where c denotes the wave speed. The waves are generated using the wave maker in the basin. Each of the wave conditions is generated at several different amplitudes, the number of amplitudes ranging from one to a maximum of four. No current is imposed. Except for case ($Fr_c = 0.80$, H/h = 0.008), all regular wave cases are measured during 40 s, where the measurements are started manually at the time when the wave maker started moving. The wave conditions are indicated in Table 2. All measurements are performed for a still water level of h = 0.489 m as maintained via an overflow boundary. The period T, the mean wave height H and standard deviation of the wave height are determined via a zero-crossing analysis where the up-crossings are used to separate between individual waves. The median wave period T of the wave gauge data for the wave gauges at x/L = 0.01, x/L = 0.14, x/L = 0.27, and x/L = 0.51 is shown in Table 2. The median is taken in order to exclude outliers. The first twenty seconds of the signals are not used in the computation
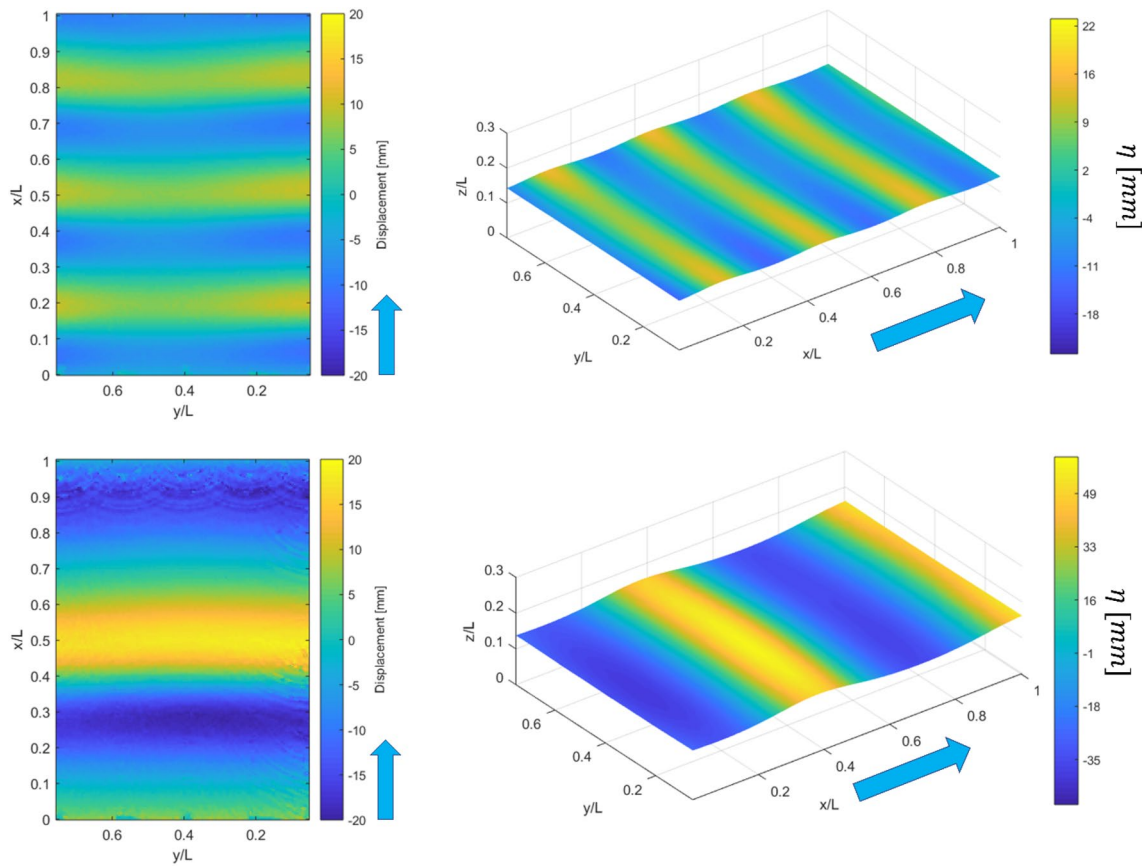
Fig. 5 Top row: condition ($Fr_c = 0.58$, H/h = 0.054) at time $t = 22.0$ s. Bottom row: condition ($Fr_c = 0.79$, H/h = 0.18) at time $t = 14.32$ s. Left: streamwise displacement field. Right: instantaneous free-surface elevation. Incident waves are propagating in the direction of positive x values

because the wave has not reached the measurement domain yet. The calculated wavelength λ_{calc} is the wavelength resulting from solving the dispersion relation ($\omega^2 = gk\tanh(kh)$) for k for the measured wave period T ($= 2\pi/\omega$) as determined from the wave gauge data, $\lambda_{calc} = 2\pi/k$. The wave speed is determined as $c = \lambda_{calc}/T$.

Wave field–monopile interaction is measured for two values of the monopile diameter-wavelength ratio, namely $D/\lambda = 0.20$ and $D/\lambda = 0.10$. It is known that monopiles only influence incident wave fields significantly when $D/\lambda > 0.20$ (MacCamy and Fuchs 1954). For these values of D/λ the interaction regime is named 'linear diffraction', for the smaller values of D/λ the monopile does not influence the incident wavefield significantly, this regime is called the 'drag-inertia regime'. The Keulegan–Carpenter number (K_C) is based on the still water level maximum velocity u_h, as estimated using linear wave theory and is defined as $K_C = u_h T/D$. For the measured cases it holds that $K_C = 0.42$ indicates that there is no separation of the flow around the monopile, whereas for case $K_C = 1.5$ there are either Honji vortices or symmetric vortices according to Mutlu Sumer and Fredsøe 2006.

The maximum uncertainty in Fr_c upon following this procedure is approximately $+0.02$ and occurs for conditions where ($Fr_c = 0.58$, H/h = 0.176) mainly due to observed wave breaking. In Appendix 2, the experimental conditions as measured for three irregular wave cases are presented.

3.2 Validation for regular waves

In Fig. 5, examples of measured displacement fields and 3D visualizations of reconstructed free surfaces are shown for wave conditions ($Fr_c = 0.58$, H/h = 0.054) at $t = 22.0$ s and ($Fr_c = 0.79$, H/h = 0.18) at $t = 14.32$ s. Some variation in the displacement over the y direction of the wave is revealed for both cases and thus immediately the benefit of wave *field* measurement methods is shown.

It is remarkable that the scattering and diffraction patterns caused by the intrusive wave gauge sensors are clearly visible in the displacement field for condition ($Fr_c = 0.79$, H/h = 0.18, Fig. 5, bottom row). In the 3D representations of the free surface for both cases, the small-scale details are less clearly visible than in the displacement fields. In Fig. 6, the temporal behavior of the free-surface level is shown at

Fig. 6 Free-surface elevation versus time for FS-SS reconstruction and wave gauge measurement at different locations for wave condition ($Fr_c = 0.58$, H/h = 0.054). Top row: x/L = 0.01. Second row: x/L = 0.14. Third row: x/L = 0.27. Fourth row: x/L = 0.51
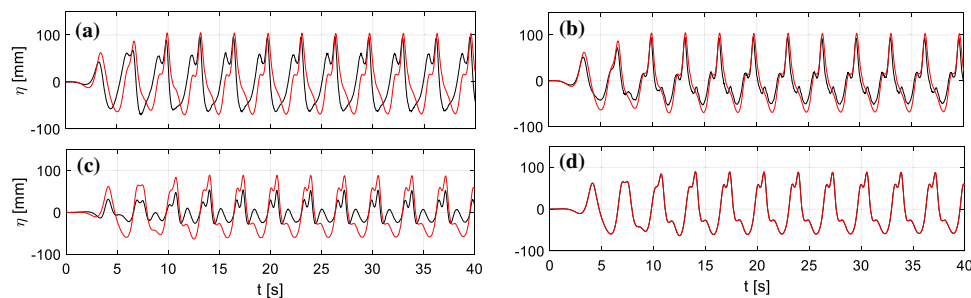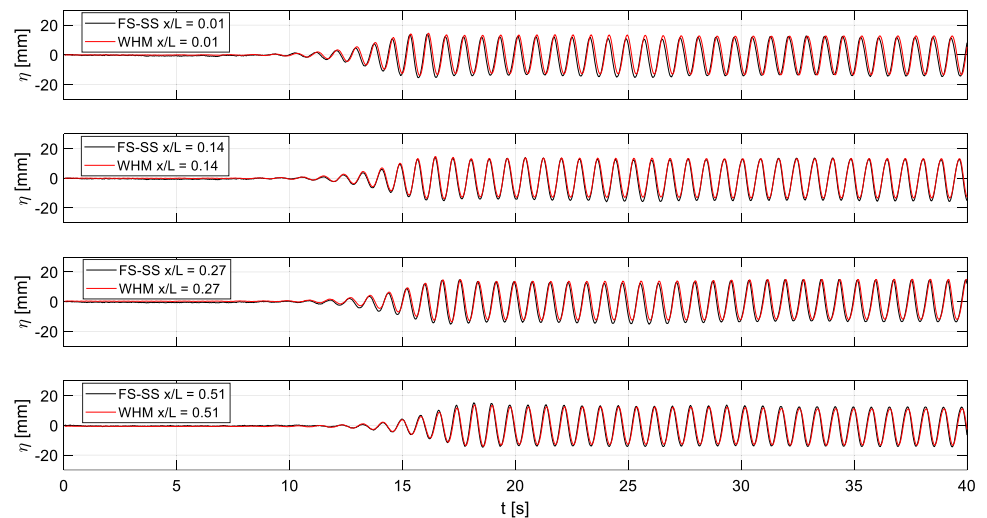
Fig. 7 Comparison of FS-SS for long wavelength case ($Fr_c = 0.97$, H/h = 0.34) between the conventional implementation of FS-SS (with assumption of zero-mean free-surface elevation) and upon the data fusion. Wave gauge signal: red line. FS-SS: black line. **a** x/L = 0.01, no data fusion. **b** x/L = 0.01, data fusion. **c** x/L = 0.51, no data fusion. **d** x/L = 0.51, data fusion

the four measurement locations for both the FS-SS reconstruction and the wave gauge measurement for wave condition ($Fr_c = 0.58$, H/h = 0.054). It is observed that the amplitude of the reconstructed wave field matches the amplitude of the wave gauge measurement well at location x/L = 0.51 (the difference being 3.3% of the wave height H) and also for the other three locations. Upon close inspection, a small phase difference of 0.04 s (1 sample) is observed for the measurement locations at x/L = 0.27 and x/L = 0.01. This phase-like error relative to the wave period is thus approximately 5% for the current case.

For the regular wave conditions with long wavelengths ($\lambda/L > 1$), the conventional implementation of FS-SS leads to unsatisfactory results with large errors, see the left panels in Fig. 7. For case ($Fr_c = 0.97$, H/h = 0.34), the amplitude difference between the FS-SS reconstruction and the wave gauge data is 34 mm (20%) on average over the locations x/L = 0.01, x/L = 0.14 and x/L = 0.27. Because of reasons unknown to the authors, the physically generated wave has a peculiar shape.

In the right panel of Fig. 7, the results for the free-surface elevation are shown upon using the sensor data fusion

for FS-SS for wave condition ($Fr_c = 0.97$, H/h = 0.34). For all locations, the amplitude difference between the FS-SS reconstruction and the wave gauge data is much smaller than in the case without using the data fusion. It can be observed that the FS-SS reconstruction indicates steeper spatial gradients than the wave gauge signal. Reasons for this are not known. On average for this case, the amplitude difference is 8% which is much smaller than upon applying the zero-mean free-surface elevation assumption.

The results for the wave height per individual wave are shown versus time in Appendix 4 in Fig. 20 for all conditions at location x/L = 0.27. For all cases where $\lambda < 0.5L$, the conventional implementation of FS-SS is used, for cases where $\lambda > 0.5L$ the sensor data fusion is used. For the conditions where $\lambda/L < 0.5$, the difference in wave height between the wave gauge data and the FS-SS measurement over time is relatively small (< 5%). For wave condition ($Fr_c = 0.58$, H/h = 0.18) regular breaking of waves is observed, this leads to minor oscillations in the corresponding FS-SS signal in Fig. 20. It is remarkable that the difference in wave height between FS-SS results and the wave gauge data is still relatively small. For the conditions where it holds that
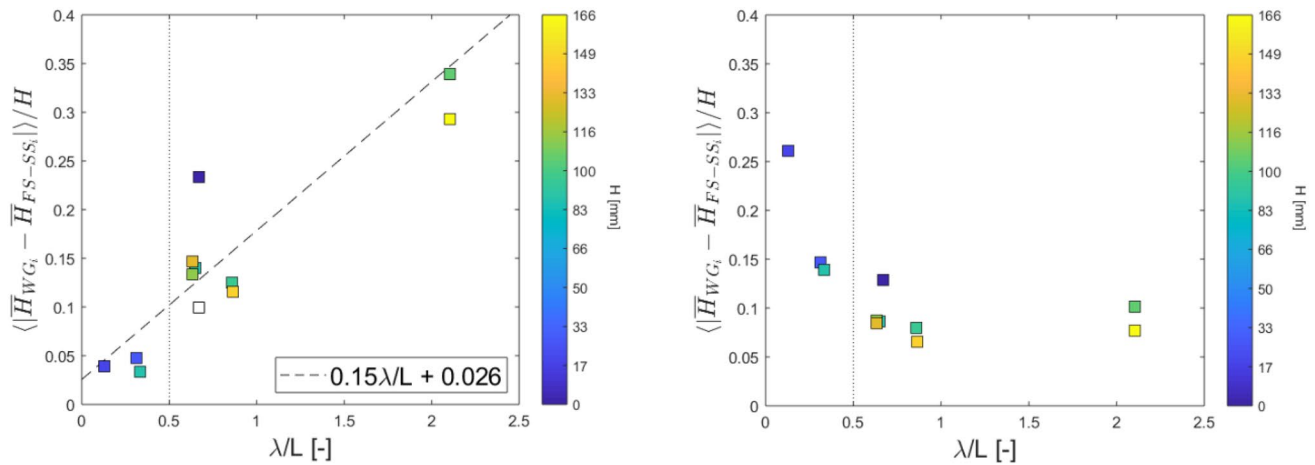
Fig. 8 Mean difference in measured wave height between wave gauge data and FS-SS reconstruction relative to wave height H, at x/L = 0.01, x/L = 0.14 and x/L = 0.27 and x/L = 0.51 versus relative wavelength. In both subfigures the dotted vertical line indicates the wavelength above which the data fusion improves the agreement between FS-SS and wave gauge data. Left subfigure: conventional implementation of FS-SS. The dashed line indicates a linear fit to the data. The marker for condition (Fr_c = 0.97, H/h = 0.34) is unreliable

because of false zero crossings in the FS-SS signal. The values for this condition are not used in the linear fit. Note that the difference for condition (Fr_c = 0.80, H/h = 0.008) is dominated by the difference at x/L = 0.01, the difference for this wave condition without using the data at x/L = 0.01 is additionally shown as a white square. Right subfigure: results for difference in measured wave height between wave gauge data and FS-SS reconstruction upon implementing the data fusion

$0.5 < \lambda/L < 1.0$ (all cases where Fr_c = 0.79 and 0.86), the difference in wave height between the wave gauge signal and the FS-SS reconstruction is more significant than for the smaller wavelength cases. The difference is between 10 and 15% except for case (Fr_c = 0.80, H/h = 0.008), where the difference is dominated by the difference at x/L = 0.01. For this case, the FS-SS time signal is additionally smoothed using a five-point moving average filter to prevent disturbance waves influencing the detection of zero-crossings.

To summarize the results, the absolute value of the time averaged difference of the intrusive measurements and the optical measurements is calculated for each of the four measurement locations. The mean of these values over the four measurement locations is shown in Fig. 8 for each wave condition (relative to the mean wave height). In the left subfigure, the conventional FS-SS processing is applied for all cases. It is found that the difference between the wave gauge data and FS-SS results increases with an approximately linear trend with wavelength except for one outlying case (Fr_c = 0.80, H/h = 0.008). No clear correlation is found for larger or smaller amplitude waves. A trend line is plotted as obtained from a linear fit. The trend indicates that the difference between the FS-SS measurement and the wave gauge measurement data increases at approximately $0.15\lambda/L + 0.026$. A general observation is that the agreement between the FS-SS measurement and the wave gauge data is better near the (streamwise) domain center than at the edge. In the right subfigure, the results upon implementing the sensor data fusion using the wave gauge signal at x/L = 0.51 is shown for all cases. Note that for case

(Fr_c = 0.37, H/h = 0.038, which is the shortest wavelength case), the wave height as measured by the wave height meter at λ/L = 0.51 has a larger amplitude than all other three sensors. This thus causes the mean difference over the four sensors to be very large. Upon analyzing the difference when using the signal of the sensor at λ/L = 0.27 in the data fusion, the difference is 11% and is in line with the results at all other wavelengths. The difference between the wave height as measured using FS-SS and the wave height as measured using the wave gauges is reduced for the cases where the wavelength over domain size is $\lambda/L > 0.5$ upon using the data fusion. This wavelength is indicated in the figure by a vertical dotted line. For the cases where $\lambda/L < 0.5$, the zero mean assumption leads to smaller differences (< 5%). It is remarkable that for these cases the difference is smaller than upon using the wave height meter signal to correct the FS-SS measurement. It is possible that making use of the signal of *multiple* wave height meters (for example as in a correction for an average, or median deviation over four locations) will lead to reduced vulnerability to outliers.

Next to the strength of quantified visualization, an advantage of the FS-SS technique lies in the instantaneous measurement over a certain spatial domain. In Appendix 3 space–time visualizations of all measured regular wave conditions are shown.

Fig. 9 Virtual displacement fields for regular wave interacting with monopile. Left: case $D/\lambda = 0.20$, time t = 12.60. Right: case $D/\lambda = 0.10$, time $t = 12.20$. Incident waves are propagating in the direction of positive x values
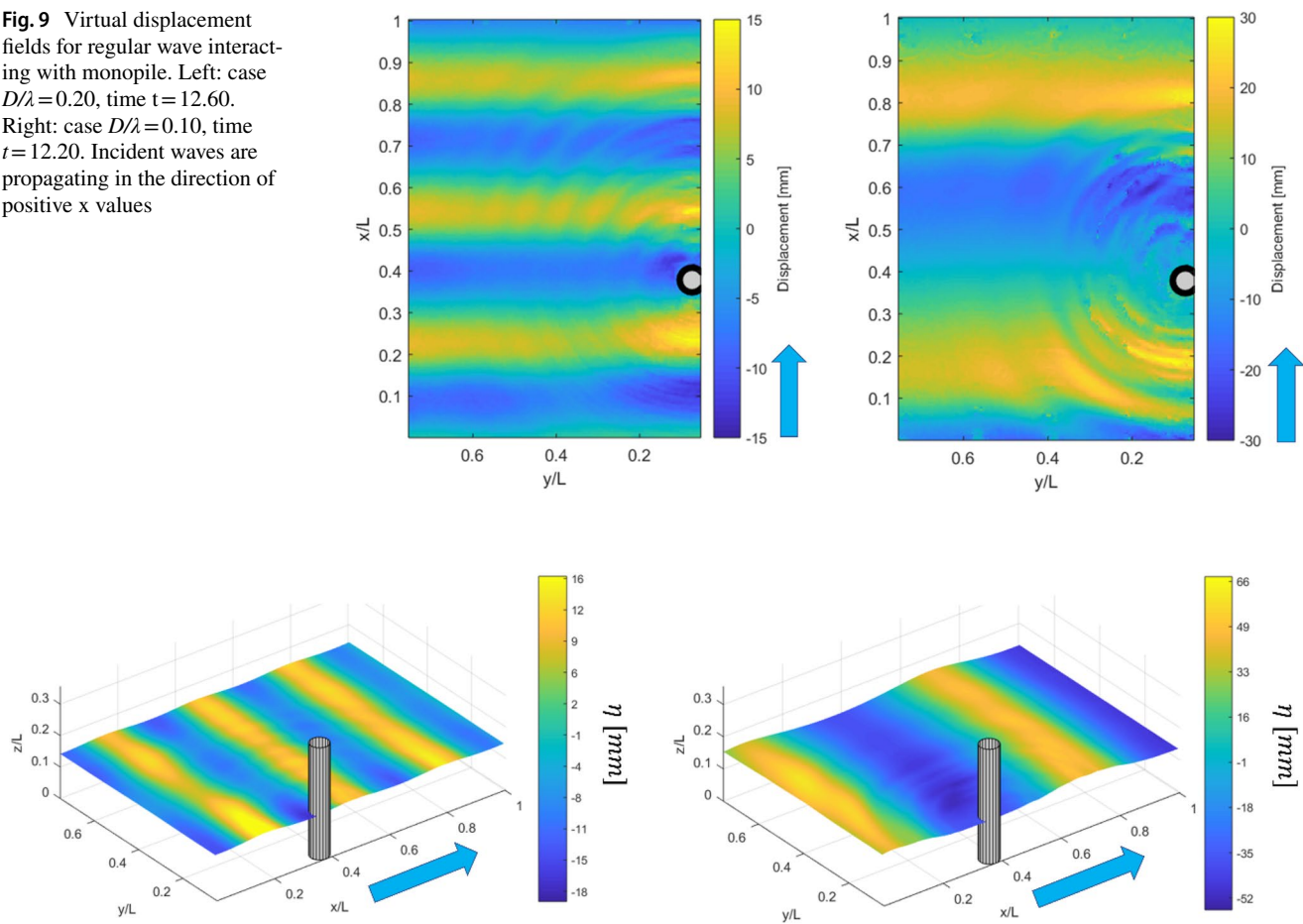

Fig. 10 3D representation of instantaneous free-surface elevation field for regular wave interacting with monopile. Left: case $D/\lambda = 0.20$. Right: case $D/\lambda = 0.10$. Incident waves are propagating in the direction of positive x values

4 Results for regular wave interaction with a monopile

4.1 Regular wave–monopile interaction

In Fig. 9, instantaneous measured virtual displacement fields are presented for wave conditions $D/\lambda = 0.20$ and $D/\lambda = 0.10$ in the presence of a monopile. In both fields, it can be observed that a circular wave pattern is generated that is centered in the monopile and that is superposed on the plane wave. In Fig. 9 (at $t = 12.60$ s for condition $D/\lambda = 0.20$ and t = 12.20 s for condition $D/\lambda = 0.10$), the circular wave that is centered in the monopile has not yet reached the boundary of the basin, so no boundary reflections are present. For the case $D/\lambda = 0.10$ some spurious displacements are observed, likely due to the steep interface or smearing of dots due to relatively fast wave interactions within the exposure time. In the figure, the edge of the monopile is shown thick to mask the area around the monopile where the image

cross-correlation possibly has spurious displacements due to the monopile.

A three-dimensional representation of the free surface as measured using FS-SS is shown for both cases in Fig. 10. A significant variation can be observed in the approaching regular wave peak over the width of the domain, where, especially close to the monopile at the side of the wavemaker, the wave amplitude is locally large. In the peaks and the throughs of the plane wave, the additional wave pattern due to reflection and diffraction by the monopile and the wave gauges is observed. In Fig. 10 also an instantaneous free surface is shown in a 3D representation for condition $D/\lambda = 0.10$. Similar to condition $D/\lambda = 0.20$, a circular diffraction pattern originating in the monopile can be observed on top of the original regular wave pattern. The modulation effect as observed for condition $D/\lambda = 0.20$ is also observed for case $D/\lambda = 0.10$, but due to the larger wavelength/domain-size ratio only one location of amplification can be observed, that is in the transverse center of the domain for the wave crest that is just entering the domain in Fig. 10.

4.2 Differential wave fields due to regular wave–monopile interaction

To compare the wave field in presence of a monopile with the wave fields in absence of a monopile it is possible to determine the differential wave field $\Delta\eta = \eta_{\text{monopile}} - \eta_{\text{no monopile}}$. In Fig. 11, the wavefields for condition $D/\lambda = 0.20$ are shown. The different columns from left to right show the wave field without monopile present in the domain, with monopile present in the domain, and the difference wave field as obtained by integrating the difference of the virtual displacement fields. The first significant generated waves are shown, the fields are displayed at an interval of 1.25 T in the subsequent rows.

Already after the first smaller waves have interacted with the monopile, a significant scattering of these waves is observed in the difference field, visible as a crescent-shaped reflection in the upstream direction, as can be observed in the top row of Fig. 11. Together with the subsequent incident wave this leads to the formation of wave amplification in a crescent shaped area upstream of the monopile. This area is indicated as the ellipsoidal dashed area in the difference field in the fifth row of Fig. 11. Note that the amplitudes of the very first generated regular waves differ slightly due to the wave generation mechanism, the later waves are highly similar. During the subsequent wave periods, this interaction pattern repeats and settles into a steady pattern, also under reflections of the large incident wavelength reflection from the wall. This behavior is reminiscent of the linear wave diffraction as described by MacCamy and Fuchs (1954) (see also Mutlu Sumer and Fredsøe 2006). In rows four and five of Fig. 11, an additional short wavelength circular diffraction wave is revealed. This radial diffraction wave continues to propagate at a lower wave speed than the incident wave and eventually also induces reflections from the wall (not visible in Fig. 11). The physical cause of the small wavelength diffraction wave is not known. Wave runup and wash-down, both at the upstream side as at the downstream side of the monopile, are a possible cause, similar to the type 1 nonlinear wave diffraction as mentioned by (Swan and Sheikh 2015). It should be noted that for the location at $\lambda/L = 0.14$ the FS-SS method overpredicts the wave height H by 20% as compared to the wave height meter, the mean difference over all four wave height meter locations is 9.5%. Despite the relatively dense grid of 14.3 mm per interrogation area, still the complex wave field might require an even higher resolution for higher accuracy as the integration likely adds some spurious diffusion. Also the optical intrusiveness of the wave height meter could explain this difference. An asymmetry in the diffraction around the monopile causes the short wavelength diffraction waves to interlock near the edge of the wake, as is indicated in the third row in Fig. 11. These waves thus form a wake structure with certain similarities to a Kelvin wave pattern, such as having a clearly discernible angle, as is indicated in the fourth and fifth row in Fig. 11. In Fig. 12, the full wave field with all mentioned phenomena is shown at approximately one wave cycle later than in the fifth row in Fig. 11. In the right subfigure of Fig. 12, the accompanying displacement field is shown where the wake angle is indicated. In the current case, the angle is 16°.

4.3 Wave breaking regime map and optical ray-crossing criterion

The wave conditions as indicated in Table 2, together with different criteria for wave breaking, are shown in Fig. 13 for the conditions without monopile present in the domain. The yellow area in Fig. 13 indicates the range in wave heights and wave periods where wave breaking should not occur according to these criteria. This area is bounded on the small period side by the wave breaking criterium based on wave steepness (Miche 1951): $H_{\text{steepness}} = 0.142\tanh(kh)\lambda$, and bounded on the large wave height side by the depth-based wave breaking criterium (assuming waves to break when the wave height is larger than 0.5 times the still water level). A criterion for the crossing of optical rays based on sinusoidal waves is given in (Moisy et al. 2009) as $H_c = \frac{\lambda^2}{2\pi^2\alpha h}$, where $\alpha = 0.24$. Two additionally generated wave conditions are indicated for which wave breaking was observed and for which no FS-SS processing is performed. On the small wave period part of Fig. 13, optical rays will cross, distorting the random dot pattern and thus rendering the image cross-correlation routine of the FS-SS procedure with a large percentage of invalid vectors. This will likely cause the resulting free-surface level to be inaccurate. Analysis of the measured image cross-correlation functions could help identify spatial zones of wave breaking.

In the current study it is found that the breaking criteria as used in Fig. 13, such as the criterion in (Miche 1951) are somewhat too mild, i.e., waves are observed to break inside the yellow region. Nevertheless, the identified FS-SS applicability region seems useful in a qualitative manner, even though there is a transition zone between breaking and non-breaking waves. It is remarkable that in the current study, the ray crossing criterion seems to indicate more accurately the breaking of waves than the steepness criterion. An additional observation is that the FS-SS method, is shown to lead to accurate results in the case of mild wave breaking (e.g., in the regular wave condition ($Fr_c = 0.58$, H/h = 0.18). Note that the regime map is valid for wave fields in absence of a structure, and that for more complex wavefields, the domain of applicability is likely decreased due to possibly steeper waves due to the interaction with the structure. When waves are relatively steep, advanced robust dot tracking techniques (e.g., see Charruault et al. 2018 and Rajendran et al. 2019)

Fig. 11 Left column: wave-fields without monopile $\eta_{\text{no monopile}}(x,y)$, center column: wavefields with monopile present $\eta_{\text{monopile}}(x,y)$, right column: difference wave fields $\Delta\eta(x,y)$. The time interval between the rows is 1.25 T. Top row: t = 7.00 s, second row from top: t = 8.00 s, third row from top: t = 9.00 s, fourth row from top: t = 10.00 s, fifth row from top: t = 11.00 s
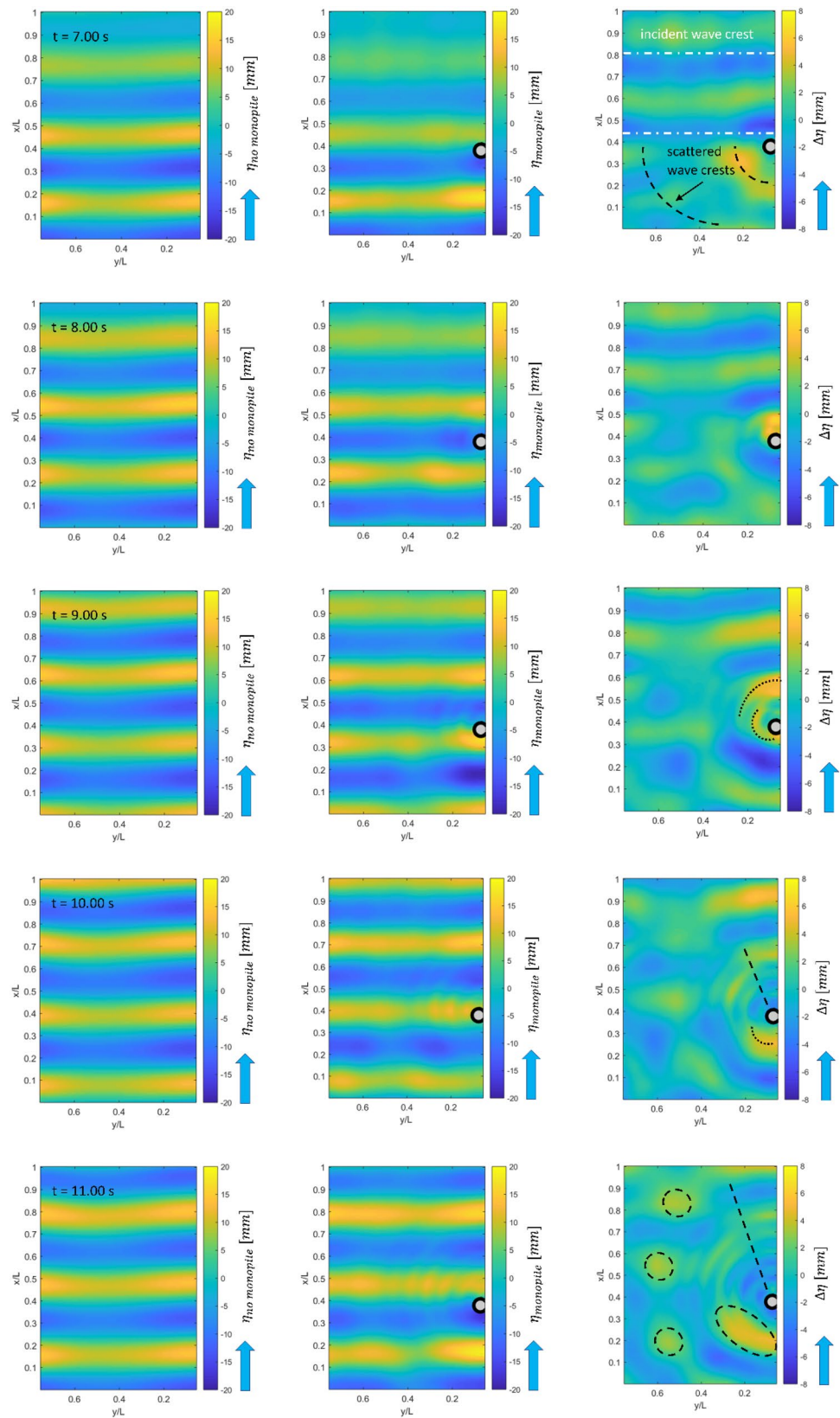
Fig. 12 Interaction between wave and monopile for case $D/\lambda = 0.20$. Left: typical wave–monopile interaction pattern. $T = 11.76$ s. Right: measured displacement difference field with wake at time $t = 11.76$ s. Incident waves are propagating in the direction of positive x values
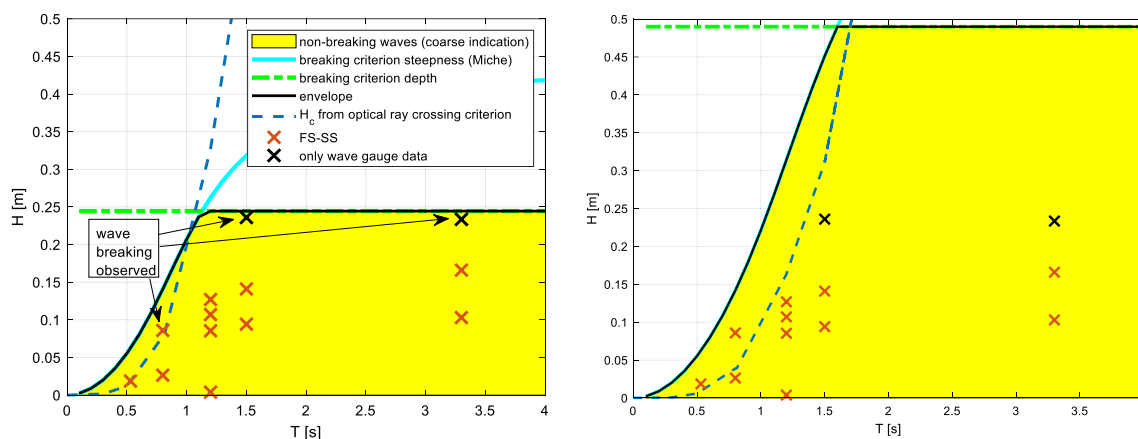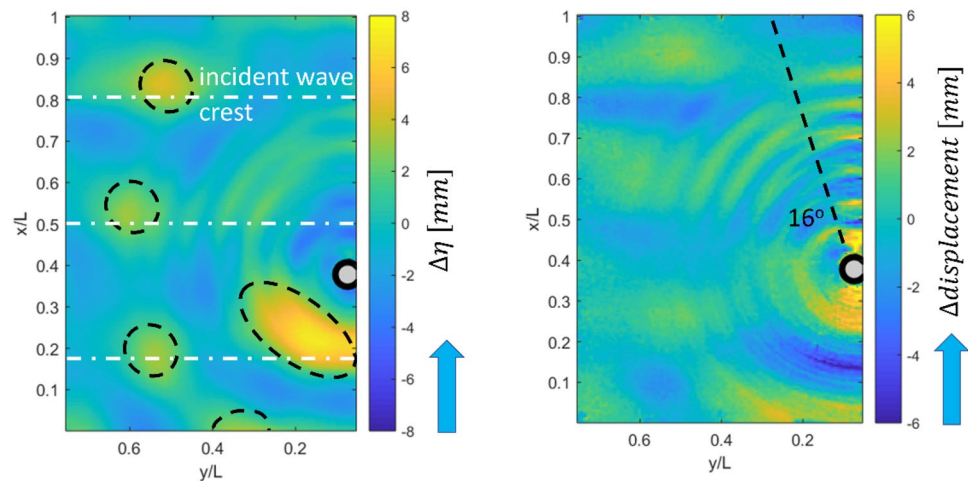
Fig. 13 Indication of regular wave conditions, regime of wave breaking and ray crossing criterion for light rays. Left: water level $h = 0.489$ m (current measurements). Right: indication of currently analyzed regular wave conditions for a hypothetical water level $h = 0.98$ m, along with the regime of non-breaking waves and ray crossing criterion for light rays

might be better suited than conventional cross-correlation techniques.

5 Conclusions

To the authors knowledge, for the first time the interaction between a regular wave field and a surface piercing cylinder, or monopile, has been measured in a domain with dimensions in the order of several m² using FS-SS. First, the FS-SS method is validated for regular wave fields of different wavelengths. It is found that for short wavelengths ($\lambda/L < 0.5$) the difference between the FS-SS measurement and wave height meter data is smaller than 5%. For wavelengths larger than half the domain size ($\lambda/L > 0.5$), the use of an additional water level measurement improves the agreement with water level sensor data considerably and leads to mean differences in wave height H, between point probes and the FS-SS reconstruction, smaller than 10%.

For the interaction between a regular wave field and a monopile, mainly the case $D/\lambda = 0.2$ is analyzed. Rich physical interaction behavior is observed, among which discrete locations of wave amplification, a small-wavelength quasi-circular diffraction pattern, and a wake structure that has certain similarities with a Kelvin wake. The regions of amplification are possibly influenced by wall reflections of the reflected incident wave, and the small wavelength diffraction pattern is possibly related to the type 1 nonlinear wave diffraction as mentioned by (Swan and Sheikh 2015). The observed large wavelength wave–monopile interaction is reminiscent of linear wave diffraction as described by MacCamy and Fuchs (1954). For case $D/\lambda = 0.1$ the domain and facility are not large enough to analyze far field wave–monopile scattering patterns. Next to the mentioned measured physical phenomena, a regime map in which both wave breaking and crossing of optical rays are indicated, is presented. From the map the applicability for certain wave conditions and still water levels can readily be deduced.

In general, free-surface measurements using FS-SS are thus attractive because of the relative ease of practical implementation of the method in hydraulic facilities without optical access from all sides or laser safety measures. Recent enhancements of the FS-SS method, such as the Bichromatic Synthetic Schlieren (Kolaas et al. 2018) are very promising but will also be harder to implement in existing large hydraulic facilities, mainly due to the necessity to generate sufficient illumination at different wavelengths and often the lack of a transparent floor in the large facilities. Possible future applications of FS-SS in domains of several m^2 could be in (research on) wave scattering on arrays of monopiles, as is relevant for off-shore platforms. Also, fundamental research in wave turbulence seems a possibility, see for example Suret et al. 2020.

For future work on free-surface measurements using FS-SS for applications in hydraulics and offshore engineering it is recommended to use high-accuracy non-intrusive point probes additionally to the optical wave field measurements, as this would minimize both optical as physical intrusivity. Secondly, advanced dot tracking techniques such as reported in for example Charruault et al. 2018 and Rajendran et al. 2019, could help improve the applicability to steeper waves. Finally, it is recommended to improve the LS integration of the free-surface gradient immediately around a structure in the domain. A possible improvement could be found in modifying the domain by adding a (numerical) boundary along the edge of the structure with accompanying boundary conditions.

Appendix 1: Description of Least-Squares integration in FS-SS

In the FS-SS method as described by Moisy et al. (2009), potential users are referred to the PIVMAT toolbox in MATLAB that is provided online at http://www.fast.u-psud.fr/pivmat/. Specifically, the function 'surfheight.m' is used to integrate the displacement field to a free-surface elevation field. In the 'surfheight.m' function the function 'intgrad2.m,' by J. D'Errico is called to integrate the free-surface gradient field. The equation describing that the gradient field is the gradient of the free surface is A $\boldsymbol{\eta}$ = grad(**f**), where in order to construct A, the derivative is approximated by central differences inside the domain, and by forward differences at the leading edge of the domain, and by backward differences at the trailing edge of the domain. The structure of the derivative matrix A is shown in Fig. 14, the matrix is not square.

See Fig. 14.

Before the system of equations is solved in a least squares way, the first component of the vector $\boldsymbol{\eta}$ is set to the mean surface height level h, and the part of the equation A
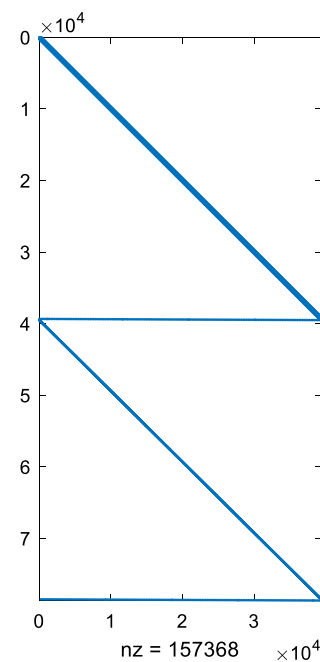

Fig. 14 Structure of derivative matrix A, as shown using MATLAB command 'spy'

$\boldsymbol{\eta}$ = grad(**f**) that can be explicitly evaluated is evaluated and subtracted from the right hand side, leaving a non-square system where matrix A has one less column than before. Now the system can be solved in a Least-Squares way using the MATLAB operator '\' which for non-square matrices uses a QR decomposition to solve the system for $\boldsymbol{\eta}$. So now $\boldsymbol{\eta}$ is the free-surface height where the point $\boldsymbol{\eta}(1,1)$ = h, the (normally constant) mean free-surface height. In case that no option saying otherwise is supplied to the function 'surfheight.m,' it will be assumed that the mean free-surface level $\boldsymbol{\eta}$ is equal to the constant free-surface height h. When there are many wavelengths in the FS-SS domain, this assumption leads to small differences with respect to wave height meter data, but in case of waves with large wavelengths, this difference can be significant.
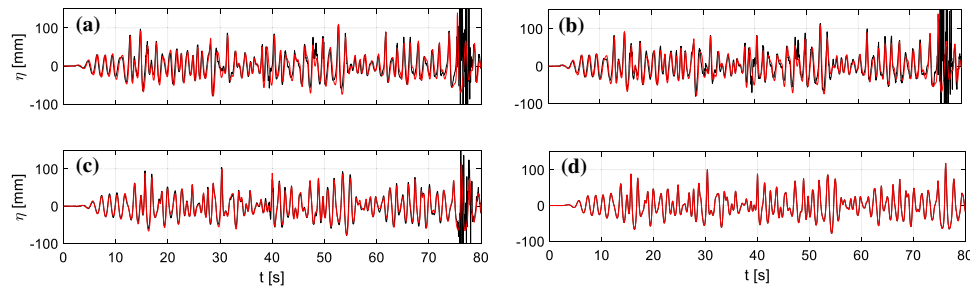
Appendix 2: Experimental conditions and results for irregular wave cases

Experimental conditions: irregular waves

In offshore engineering applications the offshore structures and scour protection systems on the seabed are tested in experimental facilities by subjecting them to a large number of scaled irregular waves representing real offshore conditions that these structures need to endure. To evaluate the applicability of the FS-SS method for physical scale experiments with offshore structures the method, with as well as
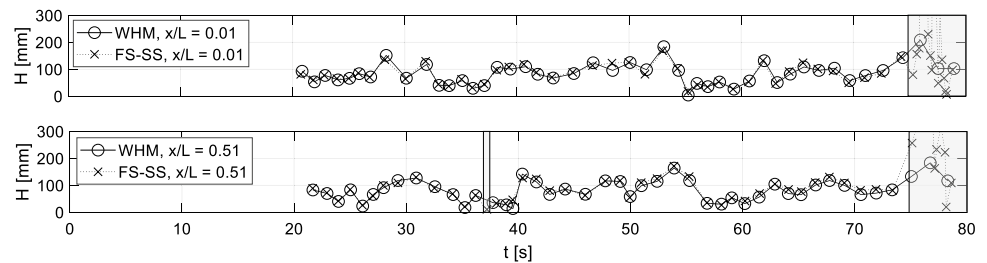
Table 3 Irregular wave conditions

Irregular wave condition	H_s [m]	T_p [s]	Time [s]
IR1	0.14	1.54	80
IR2	0.17	1.68	80
IR3	0.20	1.82	80

method performs well for the most part of the measurement for both types of integration methods of the gradient field and that the FS-SS signal seems to display spurious behavior during the time period from t = 75 s and t = 78 s. As during this time the maximum free-surface elevation is attained it is likely that this spurious behavior is caused by wave breaking and thus by a large percentage of invalid vectors in the virtual displacement field. A second smaller section

Fig. 15 Comparison of FS-SS for irregular wave condition IR1 between conventional FS-SS with assumption of zero-mean free-surface elevation and with data fusion. Wave gauge signal: red line.

FS-SS: black line. **a** x/L = 0.01, no data fusion. **c** x/L = 0.51, no data fusion. **b** x/L = 0.01, data fusion. **d** x/L = 0.51, data fusion

Fig. 16 Wave height versus inter-zero-crossing time for condition IR1 for wave gauge data and FS-SS reconstruction. Top: x/L = 0.01. Bottom: x/L = 0.51. Greyed out areas mark regions with discrepancy between results. No sensor data fusion is applied

without sensor data fusion, is tested for three irregular wave conditions. The three conditions are here referred to as IR1, IR2 and IR3. The first 80 s of the realization of each of these three conditions is analyzed. A JONSWAP spectrum is used to generate these irregular wave conditions with significant wave height and peak period as shown in Table 3, where a peak enhancement factor $\gamma = 3.3$ is used. The mean water level is the same as for the regular wave cases: h = 0.489 m.

See Table 3.

The performance of the FS-SS method for wave conditions that are often applied in offshore applications: irregular, or spectral waves is now presented.

The resulting signals at locations x/L = 0.01 and for x/L = 0.51 for condition IR1 are shown in the top left and bottom left sub images of Fig. 15 for the FS-SS processing where in the least-squares integration it is assumed that mean free-surface level is zero. In the top right sub image and the bottom right sub image of Fig. 15 the results for the same wave condition and locations are shown where the data fusion is applied. The main observations are that the FS-SS

of this spurious behavior is present near t = 37 s. Next to these observations it is noticed that the difference between the FS-SS reconstruction and the free-surface elevation as measured using a wave gauge increases with distance from the center of the field of view. Especially near the center of the domain the difference between the FS-SS reconstruction and the elevation as measured using a wave gauge is very small, this is striking especially upon realizing that it is assumed that the mean elevation is zero. In case of application of the data fusion technique as described above, the results for condition IR1 do not differ significantly from the results in case of the application of FS-SS upon assumption of the zero-mean elevation.

In Fig. 16, the wave height of the individual waves is shown over time. The difference between the wave gauge data and the FS-SS data is small. The times during which the FS-SS data shows spurious behavior due to wave breaking are marked in grey.
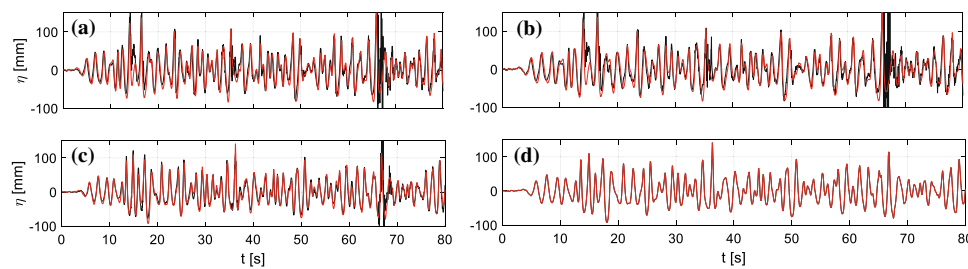
See Figs. 15 and 16.

Fig. 17 Comparison of FS-SS for irregular wave condition IR2 between conventional FS-SS with assumption of zero-mean free-surface elevation and with data fusion. Wave gauge signal: red line. FS-SS: black line. **a** x/L = 0.01, no data fusion. **c** x/L = 0.51, no data fusion. **b** x/L = 0.01, data fusion. **d** x/L = 0.51, data fusion

Fig. 18 Wave height versus inter-zero-crossing time for condition IR2 for wave gauge data and FS-SS reconstruction. Top: x/L = 0.01. Bottom: x/L = 0.51. Greyed out areas mark regions with discrepancy between results. No data fusion is applied
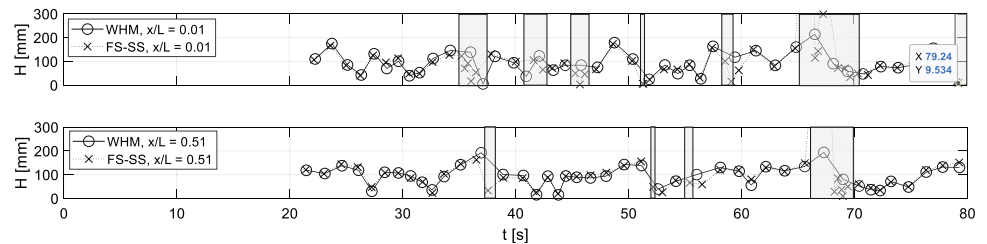
For the case of wave condition IR2, the resulting time signals are shown in Fig. 17. Qualitatively the results are comparable to the results for the IR1 case. Overall the FS-SS reconstruction performs good except for one significant section of the measurement (between t = 66 s and t = 68 s), where a relatively very large wave that breaks leads to too many spurious displacement vectors in the image cross-correlation. In a number of other smaller segments evidently spurious behavior is noticed at location x/L = 0.01 and at x/L = 0.51 but in between the FS-SS results seem good. Upon application of the sensor data fusion, the results don't differ significantly from the conventional case for the IR2. In Fig. 18 the wave height per individual wave is shown for condition IR2. The grey areas indicate times when the FS-SS results are spurious due to wave breaking in combination with non-paraxial imaging effects. For the central location there is significantly less spurious behavior in the FS-SS results.

See Fig. 17 and 18.

Qualitatively the results for case IR2 are comparable to the results for the IR1 case. The results for the irregular wave conditions are summarized in Table 4. The relative difference in wave height between the wave gauge data and the FS-SS reconstruction is < 6% of the significant wave height for conventional application of FS-SS for cases IR1 and IR2. The time where FS-SS results are unreliable due to wave breaking is < 9% for the mildest irregular wave condition and < 25% for case IR2. Due to too much wave breaking, case IR3 is not quantified currently, although possibly upon identifying and isolating the times where wave breaking corrupts the measurement and applying appropriate filtering, this case can be quantified.

See Table 4.

Discussion: Irregular waves

The measurements of the three irregular wave cases give a hint of the possible usefulness of the FS-SS method in offshore applications. Except for the case of the largest significant wave height H_s, the difference in wave height between the FS-SS results and the wave gauge data are < 6% of the

Table 4 Results for irregular wave conditions. Mean difference in wave height H between FS-SS and wave gauge data, and percentage of time where results show discrepancy between wave gauges and FS-SS results, at locations x/L = 0.01 and x/L = 0.51

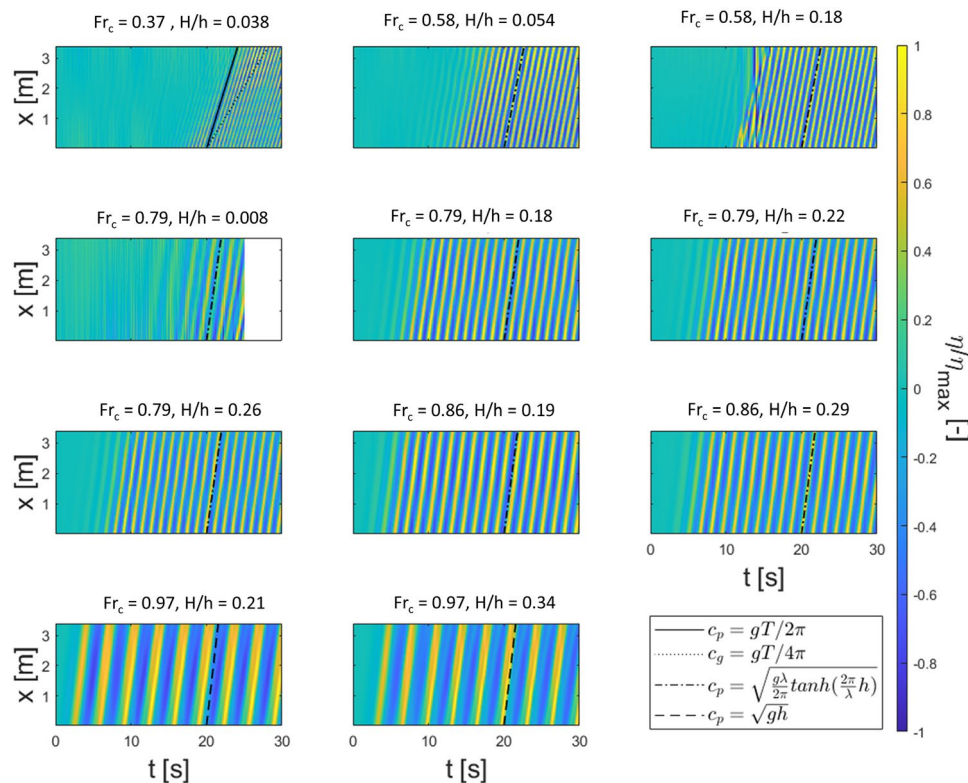| Wave condition	mean$|H_{whm}-H_{FS-SS}|$ [mm]		mean$|H_{whm}-H_{FS-SS}|/H_s$ [%]		Time fraction of wave breaking [%]	
	x/L = 0.01	x/L = 0.51	x/L = 0.01	x/L = 0.51	x/L = 0.01	x/L = 0.51
IR1	6.8	7.4	4.9%	5.3%	6.9%	8.8%
IR2	9.5	9.4	5.6%	5.5%	23%	10%
IR3	–	–	–	–	–	-

Fig. 19 Space time representation of all regular wave conditions as measured using FS-SS. For all cases where it holds that $\lambda/L > 0.5$ ($T > 1$ s) the data fusion is applied. The free-surface level in the lateral center of the FS-SS domain η is normalized with the maximum value over the space time field except for case REG3$_2$ where the maximum is selected only for $t > 20$ s because of spurious FS-SS signals due to wave breaking mostly at $t < 20$ s. Top left: $Fr_c = 0.37$. Top middle: ($Fr_c = 0.58$, H/h $= 0.054$). Top right: ($Fr_c = 0.58$, H/h $= 0.18$). Second row left: ($Fr_c = 0.79$, H/h $= 0.008$). Second row center: ($Fr_c = 0.79$, H/h $= 0.18$). Second row right: ($Fr_c = 0.79$, H/h $= 0.22$). Third row left: ($Fr_c = 0.79$, H/h $= 0.26$). Third row center: ($Fr_c = 0.86$, H/h $= 0.19$). Third row right: ($Fr_c = 0.86$, H/h $= 0.29$). Bottom row left: ($Fr_c = 0.97$, H/h $= 0.21$). Bottom row center: ($Fr_c = 0.97$, H/h $= 0.34$)

corresponding H_s during all times, except when the largest waves are present in the domain. These waves render the FS-SS method not useful during small periods because of wave breaking. In case IR1 this is approximately during 9% of time and in case IR2 this is approximately during 25% of measured time. For these irregular wave conditions it is remarkable how well FS-SS performs without the data fusion routine, which does not lead to a significant improvement for the tested irregular wave cases. For the currently tested JONSWAP wave conditions this seems to indicate that the mean water level does not vary significantly in the measurement domain. For the largest irregular wave condition, IR3, the FS-SS method seems not useful due to too much wave breaking. For the currently measured irregular wave cases, at the current water level, wave breaking is thus the main limiting factor for FS-SS, and not optical ray-crossing.

Conclusion: irregular waves

The FS-SS method has been tested and compared with wave gauge measurements qualitatively, for irregular wave fields with significant wave heights $H_s = 0.14$ m, $H_s = 0.17$ m and $H_s = 0.20$ m with peak periods $T_p = 1.54$ s, $T_p = 1.68$ s and $T_p = 1.82$ s respectively. The FS-SS method performs well (difference in H between FS-SS and wave gauge data $< 6\%$ when no wave breaking occurs) for the smallest two irregular wave cases. During each tested case the highest waves were not measurable, due to wave breaking. For the case where $H_s = 0.20$ m FS-SS is inaccurate due to too much wave breaking. In all irregular wave cases there is remarkably no significant difference between cases where the data fusion is applied and cases where the zero mean free-surface assumption is made.

Appendix 3: Space–time wave visualizations

Next to the strength of quantified visualization, an advantage of the FS-SS technique lies in the instantaneous measurement over a certain spatial domain. In Fig. 19 space–time visualizations of all measured regular wave conditions are shown where for all cases where $\lambda > 0.5L$ the data fusion is applied. At each time the instantaneous free-surface elevation at the transverse center of the domain (y = 1360 mm) normalized with its maximum value is shown. In all subfigures a line is shown that is indicative of certain relevant wave velocities. For the case $Fr_c = 0.37$, certain spatially and temporally varying elevations can be seen. The solid line that indicates the phase velocity for deep gravity waves matches well with the individual wave velocity. Less obvious but nevertheless observable is that there is a certain wave group velocity that matches with the orientation of the dotted line that indicates the group velocity of deep-water waves. For all regular wave conditions where $0.44 < \lambda/L < 1$ (0.80 s = < T = < 1.5 s) the wave velocity matches well with the dash dotted line that indicates the phase velocity

of intermediate waves ($c_p = \sqrt{\frac{g\lambda}{2\pi}\tanh\frac{2\pi}{\lambda}h}$). For case ($Fr_c = 0.58$, H/h = 0.18) some spurious behavior is observed. This is the consequence of wave breaking, leading to an invalid apparent displacement quantification. For case ($Fr_c = 0.79$, H/h = 0.008) the wave pattern is less distinguishable than for the other cases but still the wave velocity matches the phase velocity for intermediate waves. It is possible that some of the spurious behavior is caused by so-called peak locking in the image cross-correlation results. For cases ($Fr_c = 0.97$, H/h = 0.21) and ($Fr_c = 0.97$, H/h = 0.34) it is observed that when the wave enters the FS-SS domain, the wave peaks are relatively steep, and while propagating through the domain, this one peak splits into two peaks, as can also be observed in the wave gauge signals in Fig. 7.

See Fig. 19.

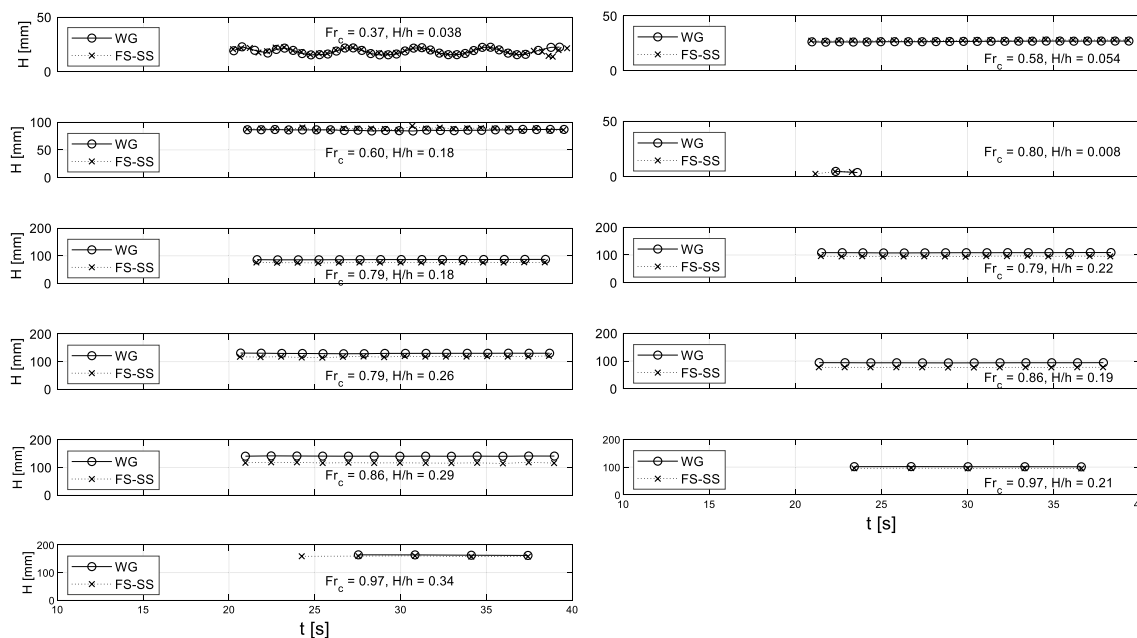# Appendix 4: Wave height signals for all cases

See Fig. 20.

Fig. 20 Wave height versus inter-zero-crossing time of the waves for wave gauge data and FS-SS reconstruction at x/L=0.27 for all regular wave conditions from zero-crossing analysis. For all cases where $\lambda < 0.5L$ the conventional implementation of FS-SS is used, for cases where $\lambda > 0.5L$ the data fusion is used

Data availability The authors are willing to share the measurement data upon request.

Declarations

Conflict of interests The authors declare that they have no conflict of interest.

Ethical approval Not applicable.

References

Adrian RJ, Westerweel J (2011) Particle image velocimetry. Cambridge University Press, UK

Benetazzo A et al (2012) Offshore stereo measurements of gravity waves. Coast Eng 64:127–138

Charruault F et al. (2018) A dot tracking algorithm to measure free surface deformations. In: *Proceedings 18th international symposium on flow visualization*. ETH Zurich

Chatellier L et al (2013) A parametric PIV/DIC method for the measurement of free surface flows. Exp Fluids 54(3):1–15

Chau FP, Eatock Taylor R (1992) Second-order wave diffraction by a vertical cylinder. J Fluid Mech 240:571–599

De Maerschalck B, Gerritsma MI (2005) The use of Chebyshev polynomials in the space-time least-squares spectral element method. Numer Algorithms 38(1–3):173–196

Gomit G et al (2013) Free surface measurement by stereo-refraction. Exp Fluids 54(6):1–11

Gomit G et al (2015) Large-scale free surface measurement for the analysis of ship waves in a towing tank. Exp Fluids 56:1–13

Gomit G, Chatellier L, David L (2022) Free-surface flow measurements by non-intrusive methods: a survey. Exp Fluids 63(6):1–25

Heller V et al (2019) Large-scale experiments into the tsunamigenic potential of different iceberg calving mechanisms. Sci Rep 9(1):1–10

Karniadakis G, Sherwin S (2005) Spectral/hp element methods for computational fluid dynamics. OUP Oxford, UK

Kolaas J et al (2018) Bichromatic synthetic schlieren applied to surface wave measurements. Exp Fluids 59(8):1–13

Li H, Avila M, Xu D (2021) A single-camera synthetic Schlieren method for the measurement of free liquid surfaces. Exp Fluids 62(11):1–15

MacCamy RC, Aam Fuchs R (1954) Wave forces on piles: a diffraction theory. US Beach Erosion Board, USA

Malenica Š, Clark PJ, Molin B (1995) Wave and current forces on a vertical cylinder free to surge and sway. Appl Ocean Res 17(2):79–90

Miche M (1951) The reflecting power of maritime structures exposed to action of swell. "Le pouvoir réfléchissant des ouvrages maritimes exposés à l'action de la houle. Ann De Ponts Et Chaussées 121:285–319

Moisy F, Rabaud M, Salsac K (2009) A synthetic Schlieren method for the measurement of the topography of a liquid interface. Exp Fluids 46(6):1021–1036

Mutlu Sumer B, Fredsøe J (2006) Hydrodynamics around cylindrical structures, vol 26. World scientific, Singapore

Paulsen BT et al (2019) Probability of wave slamming and the magnitude of slamming loads on offshore wind turbine foundations. Coast Eng 143:76–95

Proot MMJ, Gerritsma MI (2002) A least-squares spectral element formulation for the Stokes problem. J Sci Comput 17(1):285–296

Rajendran LK, Bane SPM, Vlachos PP (2019) Dot tracking methodology for background-oriented schlieren (BOS). Exp Fluids 60(11):1–13

Savelsberg R, Holten A, Van de Water W (2006) Measurement of the gradient field of a turbulent free surface. Exp Fluids 41(4):629–640

Settles GS, Hargather MJ (2017) A review of recent developments in schlieren and shadowgraph techniques. Meas Sci Technol 28(4):042001

Sheikh R, Swan C (2005) The interaction between steep waves and a vertical, surface-piercing column. J Offshore Mech Arct Eng 127(1):31–38

Soloff SM, Adrian RJ, Liu ZC (1997) Distortion compensation for generalized stereoscopic particle image velocimetry. Meas Sci Technol 8(12):1441

Stansberg CT, Kristiansen T (2005) Non-linear scattering of steep surface waves around vertical columns. Appl Ocean Res 27(2):65–80

Suret P et al (2020) Nonlinear spectral synthesis of soliton gas in deep-water surface gravity waves. Phys Rev Lett 125(26):264101

Swan C, Sheikh R (2015) The interaction between steep waves and a surface-piercing column. Philos Trans R Soc a: Math, Phys Eng Sci 373(2033):20140114

van Meerkerk M, Poelma C, Westerweel J (2020) Scanning stereo-PLIF method for free surface measurements in large 3D domains. Exp Fluids 61(1):1–16

Publisher's Note Springer Nature remains neutral with regard to jurisdictional claims in published maps and institutional affiliations.